Electric field and strain-induced band-gap engineering and manipulation of the Rashba spin splitting in Janus van der Waals heterostructures

Shubham Patel [1,*] Urmimala Dey [2] Narayan Prasad Adhikari [3] and A. Taraphder [1,†]

[1]*Department of Physics, Indian Institute of Technology, Kharagpur-721302, India*
[2]*Department of Physics, Durham University, South Road, Durham DH1 3LE, United Kingdom*
[3]*Central Department of Physics, Tribhuvan University, Kirtipur 44613, Kathmandu, Nepal*

The compositional as well as structural asymmetries in Janus transition metal dichalcogenides (J-TMDs) and their van der Waals heterostructures (vdW HSs) induce an intrinsic Rashba spin splitting. We investigate the variation of band gaps and the Rashba parameter in three different Janus heterostructures having AB-stacked MoXY/WXY (X, Y = S, Se, Te; $X \neq Y$) geometry with a Y-Y interface, using first-principles calculations. We consider the effect of external electric field and in-plane biaxial strain in tuning the strength of the intrinsic electric field, which leads to remarkable modifications of the band gap and the Rashba spin splitting. In particular, it is found that the positive applied field and compressive in-plane biaxial strain can lead to a notable increase in the Rashba spin splitting of the valence bands about the Γ point. Moreover, our *ab initio* density functional theory (DFT) calculations reveal the existence of a type-II band alignment in these heterostructures, which remains robust under positive external field and biaxial strain. These suggest novel ways of engineering the electronic, optical, and spin properties of J-TMD van der Waals heterostructures holding a huge promise in spintronic and optoelectronic devices. Detailed $\mathbf{k} \cdot \mathbf{p}$ model analyses have been performed to investigate the electronic and spin properties near the Γ and K points of the Brillouin zone.

I. INTRODUCTION

Two-dimensional (2D) transition metal dichalcogenides (TMDs) have drawn considerable attention since the discovery of graphene [1]. Endowed with several exotic and intriguing properties, such as higher stability, large spin-orbit coupling (SOC), and tunable band gap, make these materials stand out in the fields of semiconductor physics, electronics, spintronics, and valleytronics. TMD monolayers (MLs) such as MX_2, where M is the transition metal atom and X is a chalcogen atom, and numerous derivatives of TMDs have been successfully synthesized in experiments using chemical vapor deposition [2,3], mechanical exfoliation [4,5], physical vapor decomposition [6], and liquid exfoliation [7].

Breaking symmetries leads to many novel phenomena such as phase transitions, magnetism, superconductivity, and so on. Symmetries can be broken by applying electric field, strain, or stacking in different orders. In contrast to conventional TMDs, in which out-of-plane symmetry is preserved, a new class of 2D materials, Janus transition metal dichalcogenides (J-TMDs), having mirror asymmetry, are recently acquiring huge interest due to their distinct properties [8]. Janus structure (MXY; M = Mo, W; X, Y = S, Se, and Te; $X \neq Y$), based on group-VI chalcogens was introduced by Cheng *et al.* [9]. Janus monolayers (J-MLs) of MoSSe and WSSe have already been synthesized experimentally. Janus MoSSe ML

was fabricated by controlled selenization of MoS$_2$ or sulfurization of MoSe$_2$ ML [10,11], while Janus WSSe ML was synthesized by implanting Se species into WS$_2$ ML with pulsed laser ablation plasmas [12]. Contrary to usual TMDs, Janus materials display many novel properties such as Rashba effect [13–17], piezoelectric polarization [18–20], topological effects [21,22], and magnetic anisotropy [23], which make them one of the most suitable candidates for applications in spintronics, optoelectronic devices, and quantum computing.

Since 2D TMDs occupied much of the attention in the last few decades, researchers have started playing with the stacking of these materials in different layers. Efforts have been made to synthesize lateral and vertical van der Waals (vdW) heterostructures (HSs) experimentally [24–26]. Theoretically, vdW-HSs of TMDs have been investigated intensively as well. Enhanced SOC and interlayer hybridization can induce a direct to indirect band-gap transition when moving from MLs to multilayer phase [27–29] leading to novel applications [30–32]. In addition, the stacking sequence strongly influences the electronic properties and interlayer excitation within vdW HSs [33–35]. Based on J-ML TMDs with broken out-of-plane symmetry, the electronic, structural, and optical properties can be modified substantially by stacking them in different layers and constructing Janus vdW HSs [36–40].

In the search for materials with strong spin-orbit coupling (SOC), the Rashba effect appears as an important tool, resulting from the lack of out-of-plane mirror symmetry in the direction perpendicular to the two-dimensional plane. It is considered the origin of the spin Hall effect [41–44]. The capability of manipulating the Rashba effect can be exciting

*spatelphy@iitkgp.ac.in
†arghya@phy.iitkgp.ac.in

and essential for spintronic applications and making devices such as spin-FETs [45].

The Rashba effect (a momentum-dependent splitting of spin bands) for a 2D electron gas can be described by the Bychkov-Rashba Hamiltonian [14]:

$$H_R = \alpha_R(\vec{E}_{\text{int}})(\vec{k} \times \vec{\sigma}) \cdot \vec{z}, \tag{1}$$

where the factor α_R is the Rashba parameter. $\vec{\sigma}$ denotes the Pauli matrices, $\vec{k} = (k_x, k_y, 0)$ is the in-plane momentum of electrons, and $\vec{z} = (0, 0, 1)$ is the out-of-plane direction. Therefore, spin degeneracy is lifted and the energy-momentum dispersion relation takes the following form:

$$E_\pm(\vec{k}) = \frac{\hbar^2 \vec{k}^2}{2m^*} \pm \alpha_R |\Delta k|, \tag{2}$$

This relation represents two parabolas which are shifted by $\pm \Delta k$ in the reciprocal space as depicted in Fig. 3(a). Here m^* is the effective mass of the electrons.

A significant reason for the success of semiconductor spintronics is the tuning ability of Rashba spin-orbit coupling via external gating. There are several ways to tune the Rashba parameter (α_R), such as external electric field (EEF), strain, doping, etc. [46–50]. We investigate here the modification of electronic and spintronic properties of Janus vdW MoXY/WXY HSs by EEF and an in-plane biaxial strain using first-principles calculations. Our findings also shed light on the band-gap engineering and charge transfer phenomena via EEF. We outline the band-alignment facet for these HSs. Also, we present the transitions to various types of band gaps and tuning of α_R under strained conditions.

The paper is organized in the following manner. We narrate the methodology used in Sec. II. Section III A describes the crystal structure of J-TMD HSs and insights for choosing the AB stacking. In Sec. III B we study the electronic properties of three MoXY/WXY HSs, where we choose X, Y = S, Se, Te; $X \neq Y$. Our *ab initio* results are supplemented with **k** · **p** analyses in Secs. III B 1 and III B 2. This is followed by a detailed discussion of the effects of EEF and biaxial strains on band gaps and the Rashba parameter in Secs. III C and III D, respectively. Finally, we summarize our results in Sec. IV.

II. COMPUTATIONAL DETAILS

First-principles calculations are performed using density functional theory (DFT) as implemented in the Vienna *ab initio* simulation package (VASP) [51,52]. All the calculations are carried out with Perdew-Burke-Ernzerhof (PBE) [53] exchange-correlation (XC) functional in the framework of generalized gradient approximation (GGA) and projector augmented wave (PAW) method [54,55] adopted for ion-electron interactions. The cut-off energy for the plane-wave basis is set to be 500 eV, and we choose an energy tolerance criterion of 10^{-6} eV. All the structures are fully relaxed by the conjugate gradient (CG) algorithm until the force on each atom is less than 0.01 eV/Å. A Monkhorst pack of $13 \times 13 \times 1$ is used to sample the whole Brillouin zone for both geometry optimizations and static electronic structure calculations. Spin-orbit coupling (SOC) is considered in all the calculations. It is well known that the semilocal XC functionals like GGA-PBE underestimate the band gaps of semiconductors and insulators.

Therefore, in order to calculate the band gaps of the Janus HSs with better precision, we use the screened hybrid Heyd-Scuseria-Ernzerhof (HSE06) exchange-correlation functional [56,57], in which a fraction of the exact Hartree-Fock exchange is used. Our HSE06+SOC calculations are found to improve the band gaps of the HSs significantly without a noticeable change in the overall band profile. That is why in the foregoing, we present all results calculated using PBE functional unless stated explicitly.

To avoid the interactions between periodic layers, a vacuum of 20 Å is added. A DFT-D2 correction scheme developed by Grimme [58] is employed to include the van der Waals (vdW) interactions in our calculations. Phonon dispersion analysis is performed through the finite displacement method implemented in the PHONOPY code [59]. The external electric field (EEF) is applied perpendicular to the heterostructure plane by introducing a dipolar sheet at the center of the simulation cell. This method is implemented in VASP and contributed by Neugebauer and Schffler [60]. The EEF is applied to the optimized structures to avoid field-induced modifications. The structures and the charge densities are plotted in the visualization software VESTA [61].

III. RESULTS AND DISCUSSION

A. Crystal structure

In the present study we work on three vertical vdW Janus heterostructures (J-HSs), MoSSe/WSSe, MoSTe/WSTe, and MoSeTe/WSeTe. All three J-HSs consist of two different J-MLs with 2H polymorph (or trigonal prismatic phase). Although the TMDs and the J-TMDs also come with another symmetry, called 1T polymorph (or octahedral symmetric phase), the 2H phase is found to be more stable than the 1T phase [62–64] which has encouraged us to select the 2H phase for our investigations. The J-MLs possess C_{3v} point-group symmetry with space group $P3m1$ (No. 156), unlike the conventional TMDs with D_{3h} point-group symmetry and space group $P\bar{6}m2$ (No. 187). In this trigonal prismatic (2H) phase, the X and Y atoms are aligned vertically on top of each other along the z direction. The mirror symmetry in J-TMDs is broken due to different chalcogen atoms on the opposite sides of the transition metal. Stacking the MLs of J-TMDs in different layers and different orders also breaks the structural symmetry.

We first consider all possible stacking orders of J-HSs, in which the bottom layer is WXY and the top layer is MoXY (where $X \neq Y$ = S, Se, Te). The six possible stacking patterns are shown in Fig. 1. In order to have a small lattice mismatch between two monolayers, we select J-TMDs with the same X and Y chalcogen atoms. The values of the lattice mismatch are 0.03%, 0.08%, and 0.09% for MoSSe/WSSe, MoSTe/WSTe, and MoSeTe/WSeTe HSs, respectively. For all the stacking orders, similar chalcogen atoms with larger atomic numbers face each other at the interface, making the Y-Y interface, where Y is the chalcogen atom with a larger atomic number. The stacking pattern at the interface has a measurable effect on the electronic properties of the system [38]. Formation or binding energy is the difference between the total ground state energy of HS and the sum of ground-state energies of
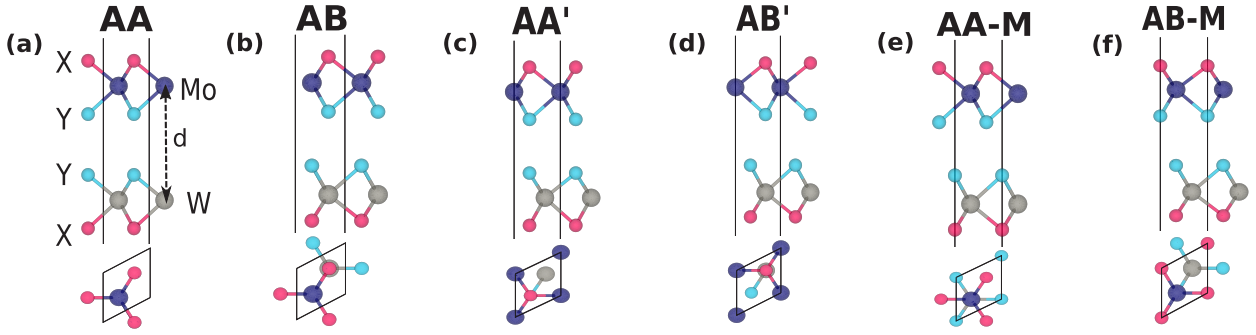
FIG. 1. Side and top views of all the stacking orders with Y-Y interface. Gray and blue spheres represent W and Mo, while magenta and cyan spheres denote X and Y chalcogen atoms, respectively. Y atom is the chalcogen atom with the larger atomic number. The interlayer distance is denoted by d.

the corresponding MLs, $E_f = E_{MoXY/WXY} - E_{MoXY} - E_{WXY}$. The negative values of the formation energies are listed in Table I, which confirm the suitability of the formation of the HSs. From our calculations and previous studies, it is found that the AB stacking with the Y-Y interface corresponds to the lowest ground state energy [39,40], making it the most stable vertical stacking. So we choose the AB-stacking geometry for HSs in our work. In the AB stacking, the chalcogen atom at the interface in the top layer is directly on top of the transition metal atom of the bottom layer, as shown in Fig. 1(b). The optimized lattice constants, interlayer distances, bond lengths, and bond angles of all three HSs with AB stacking are presented in Table I. We find that the MoSTe/WSTe J-HS has the largest interlayer distance while MoSSe/WSSe has the lowest interlayer distance for this particular AB stacking with the Y-Y interface. Calculating the electronegativity differences (Δ_{en}) for all three combinations show that the difference varies as $\Delta_{en}^{S\text{-}Te} > \Delta_{en}^{Se\text{-}Te} > \Delta_{en}^{S\text{-}Se}$, which is in accordance with their interlayer distances. Δ_{en} dictates the direction and strength of the intrinsic electric field, as described in a later section.

B. Electronic properties

In order to determine the electronic properties of AB-MoXY/WXY J-HSs, we calculate the band structures of the three vdW HSs, which are displayed in Fig. 2. The MoSSe/WSSe HS has a direct band gap at the K point of the Brillouin zone, while MoSTe/WSTe and MoSeTe/WSeTe HSs are indirect band-gap semiconductors. In MoSSe/WSSe and MoSeTe/WSeTe heterostructures, the valence band maximum (VBM) is located at the K point while it is located at the Γ point in the MoSTe/WSTe heterostructure. The conduction band minimum (CBM) in MoSTe/WSTe and MoSeTe/WSeTe HSs are positioned between K and Γ points. We also perform the band structure calculations for J-MLs and match our results with the previous studies. We find that MSSe and MSeTe (M = Mo and W) are direct band-gap semiconducting MLs, while MSTe MLs have indirect band gaps [65,66]. Among them, MoSSe ML has the largest band gap of 1.45 eV. The reduced band gap in MoSSe/WSSe and transition from direct band gap in MLs to indirect in MoSeTe/WSeTe is the result of vdW interactions between both layers of the HS as already reported in previous studies [67–69]. Since GGA-PBE functional is known to underestimate the electronic band gaps of semiconductors and insulators, we also perform HSE06+SOC calculations for the three HSs. The band gaps of all the HSs are found to be significantly enhanced with the introduction of hybrid exchange-correlation functional, as seen from Table I. The MoSSe/WSSe HS remains a direct band gap, and the other two HSs remain indirect band-gap semiconductors with HSE functional (see Fig. S1 of the Supplemental Material (SM) [70]). Figure S1 also shows that the band-gap value of the MoSTe/WSTe HS becomes larger than that of the MoSeTe/WSeTe HS, keeping the nature of band gaps unchanged, i.e., MoSTe/WSTe and MoSeTe/WSeTe HSs still remain D_4 and D_3 type band-gap semiconductors, respectively.

TABLE I. Optimized parameters, formation energies, and band gaps (both PBE and HSE) for all three AB-stacked heterostructures with Y-Y interface. The negative formation energies indicate the stability of these HSs. Symbol * represents a direct band gap.

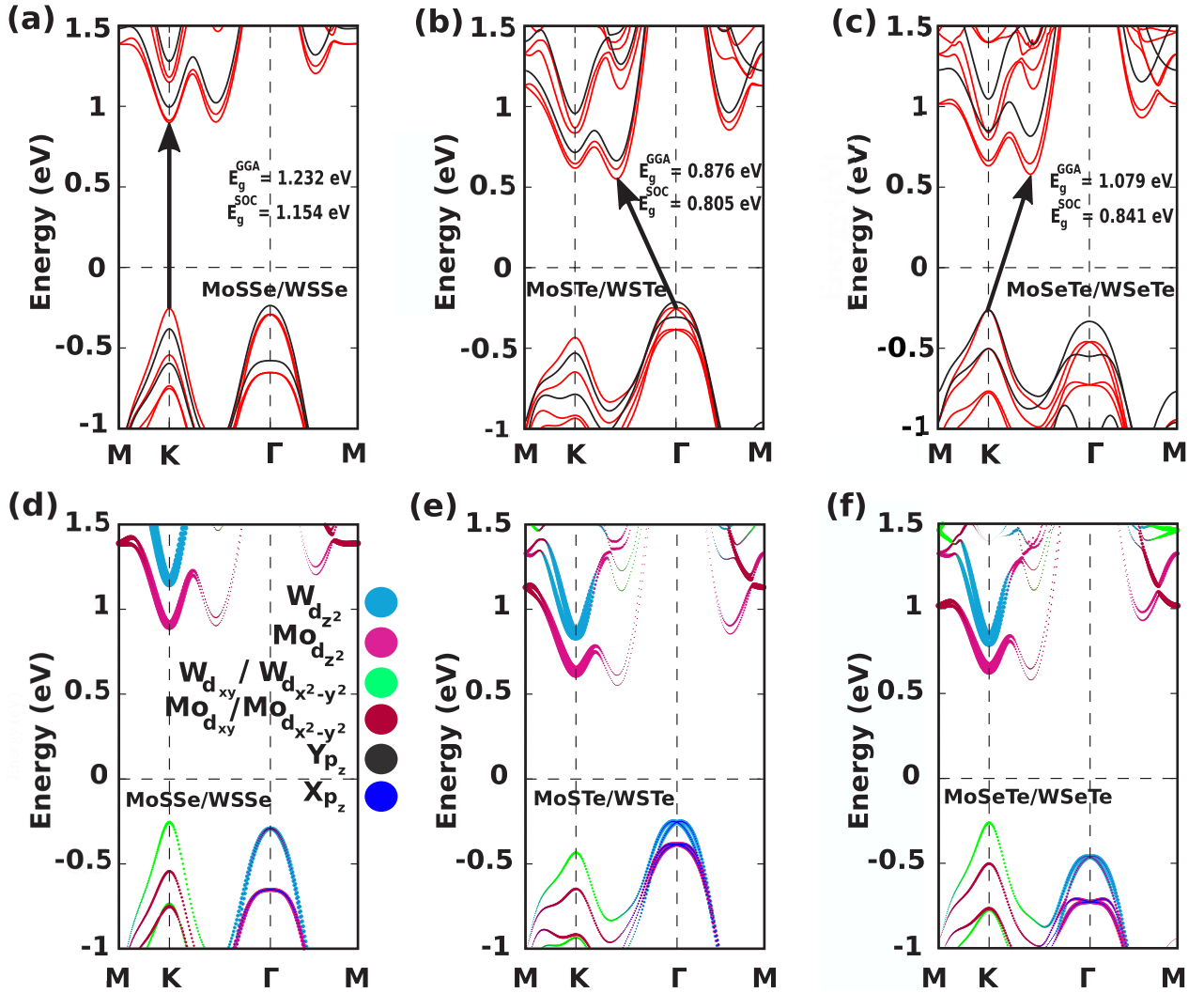| Optimized parameters	MoSSe/WSSe	MoSTe/WSTe	MoSeTe/WSeTe
Lattice constant a (Å)	3.25	3.36	3.43
Bond length Mo-X/Y (Å)	2.42/2.53	2.43/2.71	2.55/2.72
Bond length W-X/Y (Å)	2.42/2.53	2.44/2.72	2.56/2.72
Interlayer distance d (Å)	6.57	7.20	7.09
Angle X-Mo-Y	81.29°	81.58°	82.34°
Angle X-W-Y	81.46°	81.68°	82.49°
Formation energy E_f (eV)	−1.90	−2.25	−2.46
$E_g^{\text{PBE+SOC}}$ (eV)	1.154*	0.805	0.841
$E_g^{\text{HSE06+SOC}}$ (eV)	1.492*	1.207	1.149

FIG. 2. (a)–(c) Band structures of MoSSe/WSSe, MoSTe/WSTe, and MoSeTe/WSeTe J-HSs with (red) and without SOC (black) using PBE XC functional. Arrows in the figures represent the system band gaps (E_g^{SOC}) with SOC. As seen, MoSTe/WSTe and MoSeTe/WSeTe have indirect band gaps with and without SOC, while it changes from indirect to direct with the inclusion of SOC in the case of MoSSe/WSSe. M (1/2,0,0), K (1/3,1/3,0), and Γ(0,0,0) are the high symmetry points in the Brillouin zone. (d)–(f) Orbital-projected band structures of all three J-HSs. The size of the circles is proportional to the corresponding orbital weight. The orbitals weights at the VBM and CBM show that all the three HSs have type-II band alignments.

We also plot the orbital projected band structures for all three J-HSs in Figs. 2(d)–2(f). One can see that the valence band and conduction band are mainly contributed by the d orbitals of W and Mo, respectively. Moreover, the valence band maxima at the Γ and K points are primarily occupied by $W_{d_{z^2}}$ and $W_{d_{x^2-y^2}}$ (equivalently, $Mo_{d_{xy}}$) orbitals, respectively. Similarly, the conduction band minima are dominated by the $Mo_{d_{z^2}}$ orbitals. There is also a small contribution coming from the p_z orbitals of X and Y atoms, mostly away from the Fermi level. If we see the overall effect, The VBM is located at the WXY layer while the CBM is found to be at the MoXY layer, resulting in a type-II band alignment for all three HSs. The orbital symmetries of the bands and the nature of band alignment remain unchanged when we use HSE06 functional, as shown in Fig. S1. Type-II band alignment in these HSs can lead to the generation of spatially separated photoexcited electrons and holes with increasing carrier

lifetimes and thereby have immense technological importance in optoelectronics, valleytronic, photocatalytic,and photo-voltaic applications [71–74].

Janus materials with inversion asymmetry inherit a large spin-orbit coupling and thus show a large out-of-plane spin-splitting at the K point of the Brillouin zone (BZ) [75–77]. On the other hand, as a consequence of replacing one X by Y in MX_2 MLs and further with vertical stacking, additional inversion symmetry breaking takes place. Due to this inversion asymmetry, these J-MLs and J-HSs inherit an intrinsic electric field which is the main source of the emerging in-plane Rashba spin splitting [14]. The net transverse electric field mainly controls the strength of this Rashba spin splitting. The schematics to calculate the α_R is presented in Fig. 3(a), which is defined as $\alpha_R = 2E_R/k_R$. Here E_R is the Rashba energy, and k_R is the momentum offset around the Γ point, also called the Rashba wave vector. The calculated values of α_R for three
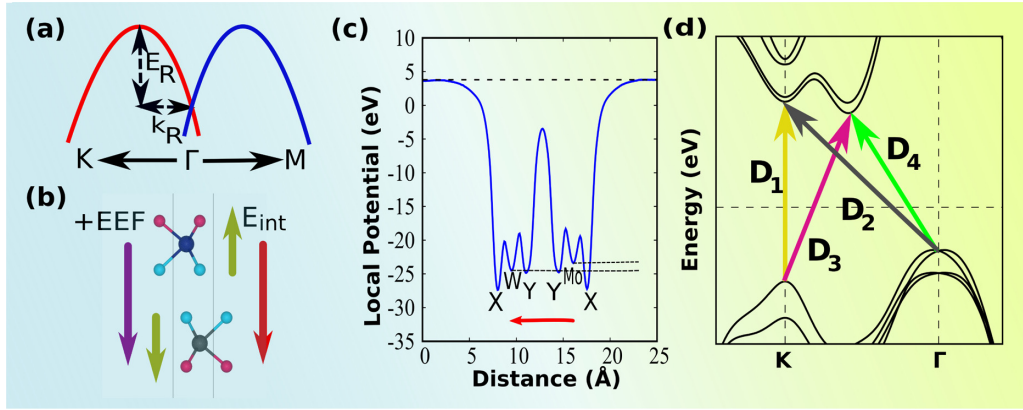
FIG. 3. (a) Schematics of calculating the Rashba parameter α_R, where E_R is the Rashba energy and k_R is the momentum offset. (b) Directions of the intrinsic and external electric fields. E_{int}, with the red arrow, represents the net intrinsic electric field, and olive green arrows denote the intrinsic fields due to the chalcogen atoms in each layer. +EEF is the positive external electric field applied in the downward direction from the MoXY layer to the WXY layer. (c) Local electrostatic potential profile for MoXY/WXY HS without any external effect. The red arrow represents the direction of E_{int}. Here the dashed lines indicate the potential drop across the interface, confirming the existence of an intrinsic electric field in the direction from Mo to W atom. (d) A general band structure showing different types of gaps between the valence band and the conduction band. D_1 is the direct gap at the K point, D_2 is the gap between VBM at Γ and CBM at the K point, and D_3 (D_4) is the gap between VBM at K (Γ) and CBM in the Γ-K direction. Out of these four gaps, one of them turns out to be the energy band gap of the system.

HSs, MoSSe/WSSe, MoSTe/WSTe, and MoSeTe/WSeTe are 30.74, 178.8, and 129.8 meV Å, respectively.

We list the values of α_R for different Janus systems in Table S1 [70], which shows that Rashba spin splittings depend upon the interfacial (or interlayer) distance, structural arrangements, and the strength of the net intrinsic electric field. α_R is found to be highest for AA stacking with the Y-Y interface. This particular stacking with the said interface has the intralayer dipoles in opposite directions, which results in an increase of the interlayer distance between the transition metals. As a result, the net intrinsic electric field due to the transition metals becomes larger, giving rise to a large spin splitting. On the other hand, α_R has the lowest values for AB-stacked Y-X interfaces having the smallest interfacial distance. As mentioned earlier, in the present work we choose the Janus HSs, which possess the most stable interface structure (Y-Y) and stacking pattern (AB stacking) and correspond to the correct configuration, which is most likely to be realized in experiments. Our chosen systems have lower α_R compared to the Janus monolayers, X-Y interfaced bilayers and AA-stacked HSs due to the cancellation of intrinsic electric fields originating from the chalcogen atoms on each layer, leaving behind contributions from the transition metals only. We will discuss this in Sec. III C in more detail. Moreover, a detailed investigation (from Table S1) reveals that for a given interface, α_R varies as $\alpha_R^{MoSTe/WSTe} > \alpha_R^{MoSeTe/WSeTe} > \alpha_R^{MoSSe/WSSe}$ for AB stacking and for AA stacking it varies as $\alpha_R^{MoSeTe/WSeTe} > \alpha_R^{MoSTe/WSTe} > \alpha_R^{MoSSe/WSSe}$. Therefore, to have promising technological applications, it is essential to modify the strength of the Rashba spin splitting in these HSs by external perturbations. In order to investigate the electronic properties at the Γ and K points of the BZ in detail, we define $k \cdot p$ Hamiltonians in the following.

1. $k \cdot p$ Hamiltonian at Γ point

The Janus HSs possess C_{3v} point group symmetry in which a center of inversion is absent. Absence of inversion symmetry in these 2D materials gives rise to a momentum dependent Rashba spin splitting [14]. In our electronic structures, Rashba-like spin splitting is observed only around the Γ point, as seen from Fig. 3(a). At this high symmetry point (Γ), the allowed linear-in-k term in the $k \cdot p$ Hamiltonian is ($k_x\sigma_y - k_y\sigma_x$) [14,78]. Other higher-order terms are also present [78–80], which are cubic in k. The $k \cdot p$ Hamiltonian around Γ subjected to spin-orbit coupling can be defined as follows:

$$H(k)^\Gamma = H_0(k) + \alpha_R(k_x\sigma_y - k_y\sigma_x) + \beta_R\big[\big(k_x^3 + k_xk_y^2\big)\sigma_y$$
$$- \big(k_x^2k_y + k_y^3\big)\sigma_x\big] + \gamma_R\big(k_x^3 + 3k_xk_y^2\big)\sigma_z$$
$$\approx \big(Ak_x^2 + Bk_y^2\big) + \alpha_R(k_x\sigma_y - k_y\sigma_x), \quad (3)$$

where $H_0(k)$ is the free electron Hamiltonian; $A = \frac{\hbar^2}{2m_x^*}$ and $B = \frac{\hbar^2}{2m_y^*}$ with m_x^* and m_y^* being the effective masses of electrons along different directions. α_R is the Rashba parameter in linear order, and β_R and γ_R are the coefficients in the cubic order.

We ignore the small cubic Rashba terms in the Hamiltonian and numerically fit the first-principles bands around the Γ point. One can see from Figs. 4(a)–4(c) that the eigenvalues of the Rashba Hamiltonian excellently fit the DFT bands around the Γ point. From the numerical fit, we obtain the values of the α_R for the three Janus HSs, which are in agreement with the DFT values and listed in Table S2 [70].

In order to show the spin orientations for the two bands around Γ, we have plotted the spin textures in the momentum space, as shown in the middle and lower panels of Fig. 4. The out-of-plane spin projection (S_z) is indicated by the background color. We observe circular spin textures for the
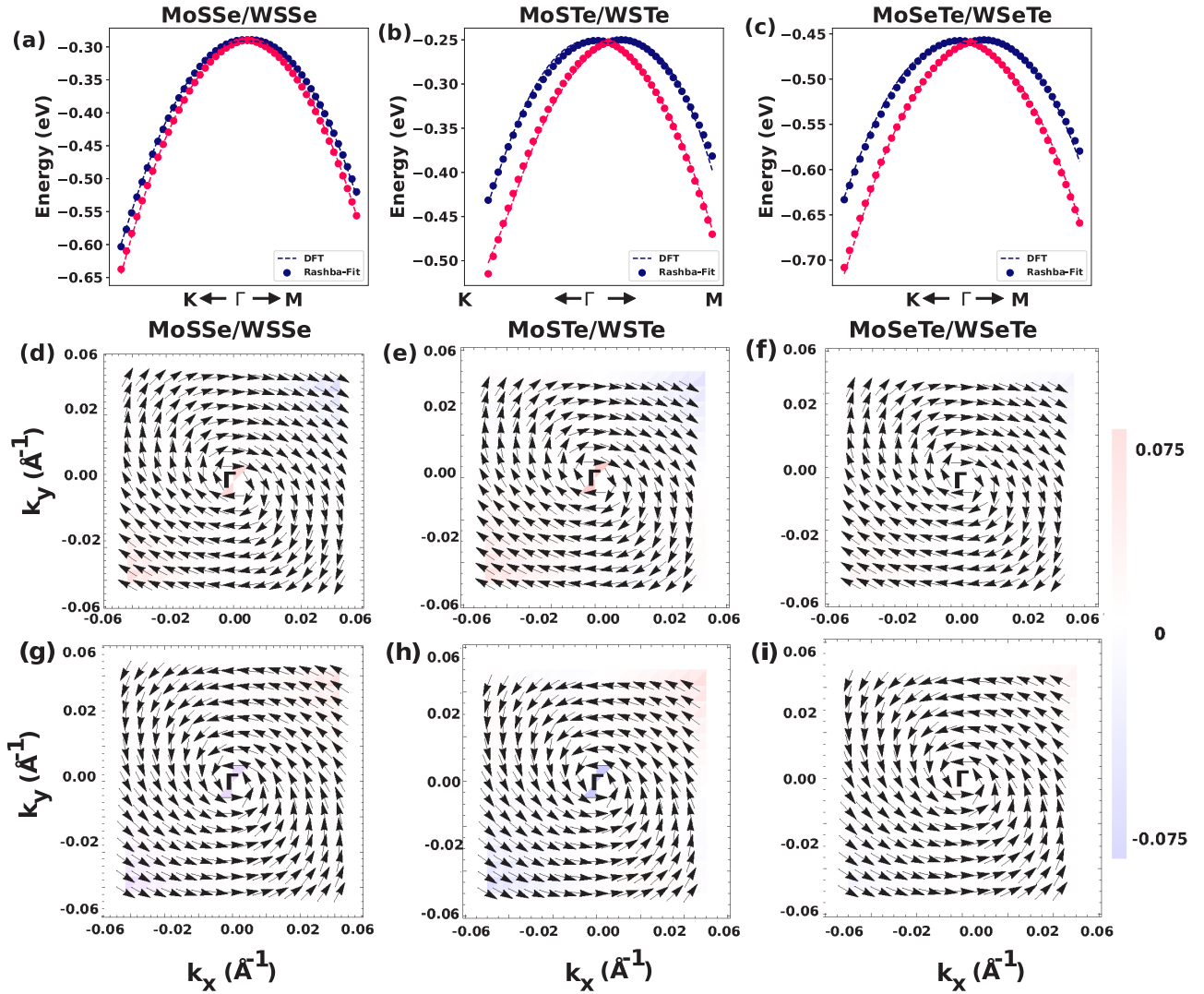
FIG. 4. (a)–(c) Bands around Γ point fitted along $\frac{2\pi}{a}(0.08, 0.08, 0) - (0, 0, 0) - \frac{2\pi}{a}(0.12, 0, 0)$ direction (along K-Γ-M) of the Brillouin zone, where a is the in-plane lattice constant. The dashed lines and scattered points represent the DFT bands and the $k \cdot p$ bands, respectively. (d)–(f) Spin textures for the inner branch (red bands in the upper panel). (g)–(i) Spin textures for the outer branch (blue bands in the upper panel). The color bar on the right shows the magnitude of the out-of-plane spin projection (S_z). The almost colorless backgrounds in the middle and bottom panels depict the 2D nature of Rashba spin splitting around the Γ point.

outer (blue bands in the upper panel) and inner (red bands in the upper panel) branches which encircle in opposite directions. Moreover, the almost colorless backgrounds in the spin textures indicate the presence of negligible out-of-plane spin components. Opposite spin orientations of the inner and outer branches and the presence of negligible out-of-plane spin components are the characteristic features of the pure Rashba effect [81]. Therefore, from this analysis, it is evident that the bands around the Γ point are best described by the Rashba-type Hamiltonian given in Eq. (3). Although very small, the presence of a weak out-of-plane projection explains a slight mismatch in the numerical values of α_R obtained from DFT and numerical fittings.

2. $k \cdot p$ Hamiltonian at K point

While the electronic and spin properties of MoSTe/WSTe HS with VBM at Γ are dictated by the Rashba Hamiltonian described above, the properties near the K point are also exciting and mainly crucial for MoSSe/WSSe and MoSeTe/WSeTe HSs for which the VBM lies at the K point. The valence band maxima and conduction band minima at the K point in both MoSSe/WSSe and MoSeTe/WSeTe HSs are contributed by $d_{xy} + d_{x^2-y^2}$ and d_{z^2} orbitals of transition metals (both Mo and W), respectively. Therefore, the symmetry adapted basis functions at the band edges are [75]

$$|\phi_c\rangle = |d_{z^2}\rangle, \quad |\phi_v\rangle = \frac{1}{\sqrt{2}}(|d_{x^2-y^2}\rangle + i|d_{xy}\rangle), \quad (4)$$

where the subscripts v and c indicate the valence band and the conduction band, respectively. Spin-orbit coupling removes the spin degeneracy at VBM and CBM and results in two spin-split bands (total four bands) below and above the Fermi level for a single layer. However, the orbital symmetries of the bands remain preserved, as seen from Figs. 2(d)–2(f). The MXY (M = transition metal) layers have the similar orbital
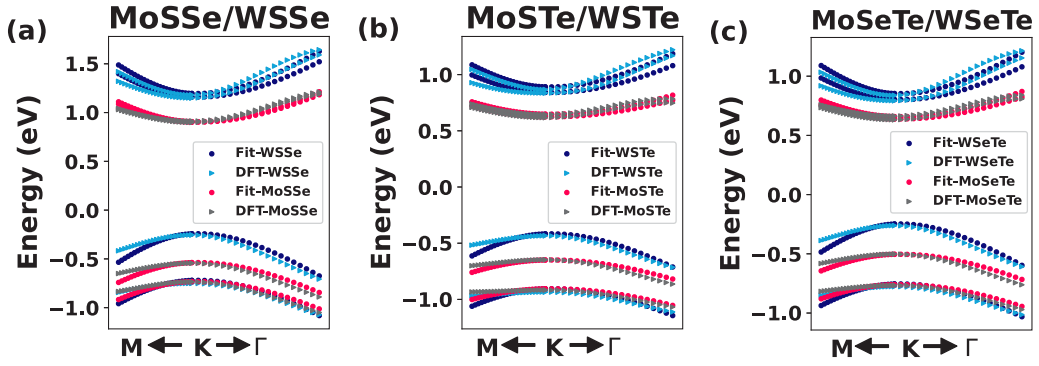
FIG. 5. Band structures for (a) MoSSe/WSSe, (b) MoSTe/WSTe, and (c) MoSeTe/WSeTe around the K point are fitted along the $\frac{2\pi}{a}(0.38, 0.25, 0) - \frac{2\pi}{a}(0.33, 0.33, 0) - \frac{2\pi}{a}(0.25, 0.25, 0)$ direction (along M-K-Γ) of the Brillouin zone, where a is the in-plane lattice constant. Right triangles represent the DFT bands and circles denote the $k \cdot p$ bands in Eq. (5).

contributions at K and K' valleys except for the fact that the spin is flipped at another valley. It also emphasizes that the spin splitting does not depend on the model details and for the present study we only focus on the spin properties at K valley.

A minimal four-band $\mathbf{k} \cdot \mathbf{p}$ Hamiltonian with SOC can be constructed for each layer at the K point as [75]

$$H(k)^K = at(k_x\sigma_x + k_y\sigma_y) + \frac{\Delta}{2}\sigma_z + \lambda_v\frac{1 - \sigma_z}{2}\hat{s}_z$$
$$+ \lambda_c\frac{1 + \sigma_z}{2}\hat{s}_z, \tag{5}$$

where a, t, $2\lambda_v$, and $2\lambda_c$ are the lattice constant, hopping integral, and spin splittings at the valence band top and conduction band minimum, respectively. Here $\hat{\sigma}_z$ are the Pauli matrices for the basis functions, while $\hat{s}_z$ are the spin Pauli matrices. Δ is the direct energy gap between the VBM and CBM of respective MXY layers at the K point. The third and fourth terms in the Hamiltonian remove the degeneracy at the valence band and the conduction band, respectively.

We fit this Hamiltonian with our DFT bands at K [Figs. 5(a)–5(c)] and extract the parameters for each layer separately. The extracted values of the parameters are in excellent agreement with the DFT parameters, as listed in Table II. The spin splittings at the top of valence bands (λ_v) are larger than the splittings at the conduction band minima, which is known for a while for normal TMDs [75,76]. Also, the splittings for WXY layers in the valence band are almost double of that for the MoXY layers, which is related to the fact that the SOC is larger for the heavier atoms. It is important to note

that MoSTe/WSTe and MoSeTe/WSeTe HSs are not direct band-gap semiconductors. However, for the purpose of fitting, we have considered the conduction bands in the DFT band structures, which represent the D_1 type gap (direct band gap) at the K point. The extracted parameters, which are in very good agreement with the DFT bands, show that our band structure near the K point can be safely described by the $k \cdot p$ Hamiltonian defined by Xiao *et al.* [75].

C. Effects of external electric field

As mentioned in the previous section, with the effect of mirror asymmetry in J-HSs, a vertical dipole moment is formed, which causes an intrinsic out-of-plane electric field, leading to the novel properties that are absent in conventional MX_2 ML TMDs. It is possible to enhance or reduce the strength of the intrinsic electric field by applying an external electric field (EEF), either parallel or antiparallel to it. The net electric field can then modify the Rashba splitting as well as the orbital overlaps resulting in the variation of band gaps. There are many studies dedicated in this field, varying from bulk [46] to 2D materials [47,65,79,82] and to the HSs [83]. Variation of the band gaps and the Rashba parameter α_R with external electric field in the case of J-MLs has been studied by Hu *et al.* [65].

Here we first study the evolution of different types of band gaps and their tuning with EEF. Since we have AB-stacked HSs with a Y-Y interface, where the electronegativity of the Y atom is less than that of X, the intrinsic electric field is

TABLE II. Values of the parameters in Eq. (5) obtained by fitting the first-principles bands around K. a, t, Δ, $2\lambda_v$, and $2\lambda_c$ are the lattice constant, hopping integral, band gap, and spin splittings at the VBM and CBM, respectively. Both the MXY layers (M = transition metal) are treated individually to perform the numerical fitting. Δ is the direct energy gap between the VBM and CBM of respective MXY layers.

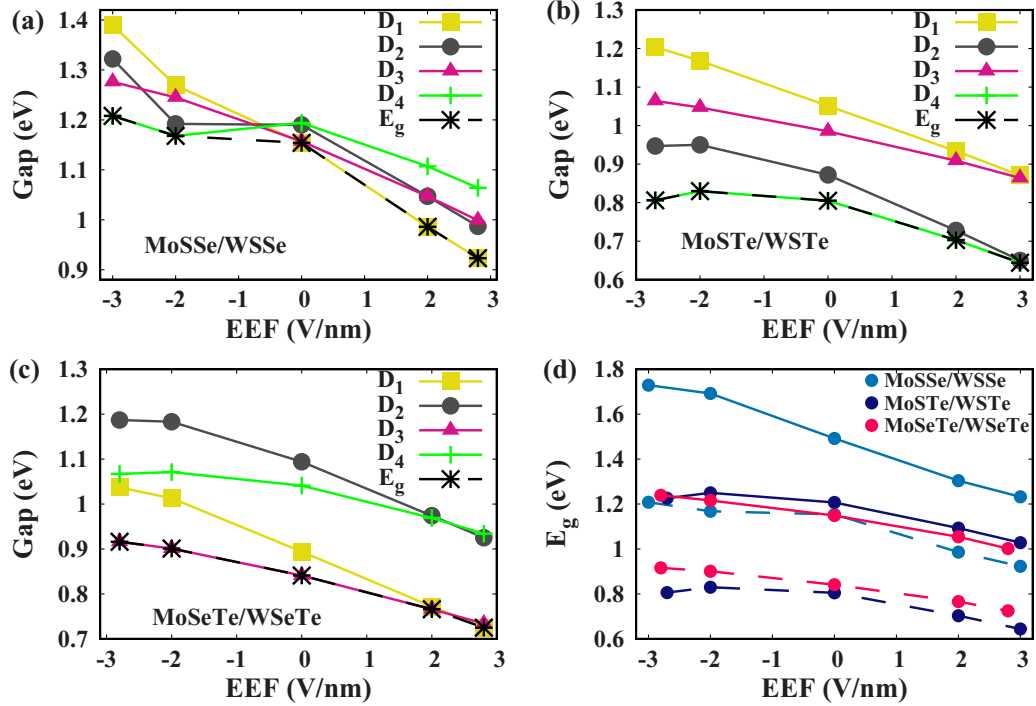| Parameters	Fitted			DFT(GGA-PBE)		
	MoSSe (WSSe)	MoSTe (WSTe)	MoSeTe (WSeTe)	MoSSe (WSSe)	MoSTe (WSTe)	MoSeTe (WSeTe)
a	3.25	3.36	3.43			
t	0.99 (1.21)	0.67 (0.93)	0.73 (0.96)			
Δ	1.54 (1.66)	1.41 (1.53)	1.28 (1.33)	1.40 (1.44)	1.26 (1.27)	1.13 (1.05)
$2\lambda_v$	0.19 (0.48)	0.26 (0.49)	0.26 (0.51)	0.19 (0.49)	0.27 (0.50)	0.26 (0.51)
$2\lambda_c$	0.01 (0.04)	0.02 (0.05)	0.02 (0.05)	0.01 (0.03)	0.03 (0.03)	0.03 (0.04)

FIG. 6. (a)–(c) Variation of gaps with EEF for MoSSe/WSSe, MoSTe/WSTe, and MoSeTe/WSeTe HSs, respectively. D_1 is the direct gap at the K point, D_2 is the gap between VBM at Γ and CBM at the K point, and D_3 (D_4) is the gap between VBM at K (Γ) and CBM in the Γ-K direction, as shown in Fig. 3(d). E_g is the true energy band gap indicated by black dashed lines. (d) System band gaps (E_g) with HSE06 (solid lines) and GGA-PBE (dashed lines) functionals.

directed from Y to X. It is the opposite in both layers, which cancels the net polarization induced by the chalcogen atoms. However, the transition metal atoms in both layers have different electronegativities. As a result, there is a small intrinsic electric field induced from Mo to W atom [see Fig. 3(b)]. This direction of the induced electric field can be verified from the local electrostatic potential profile in Fig. 3(c), in which a potential drop is clearly visible.

The troughs in the local potential plot for W and Mo are not at the same height, and it indicates that there is an intrinsic electric field in the direction from Mo to W atom. Now, if EEF is applied in the direction of the intrinsic field, it superimposes and shows us the modified effects in band gaps and α_R as well. We apply the positive EEF in the direction from Mo to W as shown in Fig. 3(b). As discussed above, among all three HSs, MoSSe/WSSe has a direct band gap at the K point, while the other two HSs have indirect band gaps. The nature of the gap varies with EEF, and in most cases, it is indirect. The different types of gaps with PBE XC functional are illustrated in Fig. 3(d). The MoSSe/WSSe HS shows a direct band gap of D_1 type in the positive EEF case while it is of D_4 type indirect band gap in the reverse EEF. On the other hand, the nature of the band gap in the case of MoSTe/WSTe does not change with EEF, and it remains the D_4 type throughout. At 0.28 V/Å, in the MoSeTe/WSeTe HS, there is a transition from D_3 type band gap into a direct band-gap (D_1) semiconductor. The modulation of different kinds of gaps with EEF, along with the total system band gap, is demonstrated in Fig. 6. We can clearly see the band gaps reduce with the strength of EEF, and the reason one can think of is the charge transfer from the upper (MoXY) layer to the bottom (WXY) layer.

Charges try to align them in the direction of an electric field. Thus, as we increase EEF in the direction of the intrinsic electric field, there is more charge accumulation on the WXY layer of the HSs. This charge transfer increases the interaction between both layers leading to the band-gap reduction. The HSE06 XC functional does not change the qualitative nature of the bands for MoSTe/WSTe and MoSeTe/WSeTe HSs except for an increment in the band-gap values, as shown in Fig. 2. They remain indirect band-gap semiconductors of D_4 (MoSTe/WSTe) and D_3 (MoSeTe/WSeTe) type for all values of EEF. On the other hand, MoSSe/WSSe HS remains a direct band-gap semiconductor of D_1 type in the reverse EEF up to -0.2 V/Å and then converts to D_3 type (see Fig. S2(a) [70]).

We can also verify from the charge density plots that without the application of any EEF, there is more charge localization on the WXY layer; this further clarifies the direction of the intrinsic electric field, which is downward. The layer projected band structures in Fig. 7 are in accordance with the charge density plots, and it can be confirmed that in the reverse EEF, the VBM at the Γ point is occupied by the MoXY layer, unlike the case of zero and positive EEF where it is occupied by WXY layer. The CBM at K point is occupied by the MoXY layer in case of positive EEF, while there is a mix contribution from both the layers at CBM, which is now located in between the Γ and K points, in the reverse EEF strength. This indicates that the type-II band alignment in the pristine HSs remains robust under a positive electric field, whereas the nature of the band alignment changes by the application of a reverse electric field.

The effect of EEF on α_R is summarized in Fig. 8. It can be noted that α_R is zero under reverse EEF for the
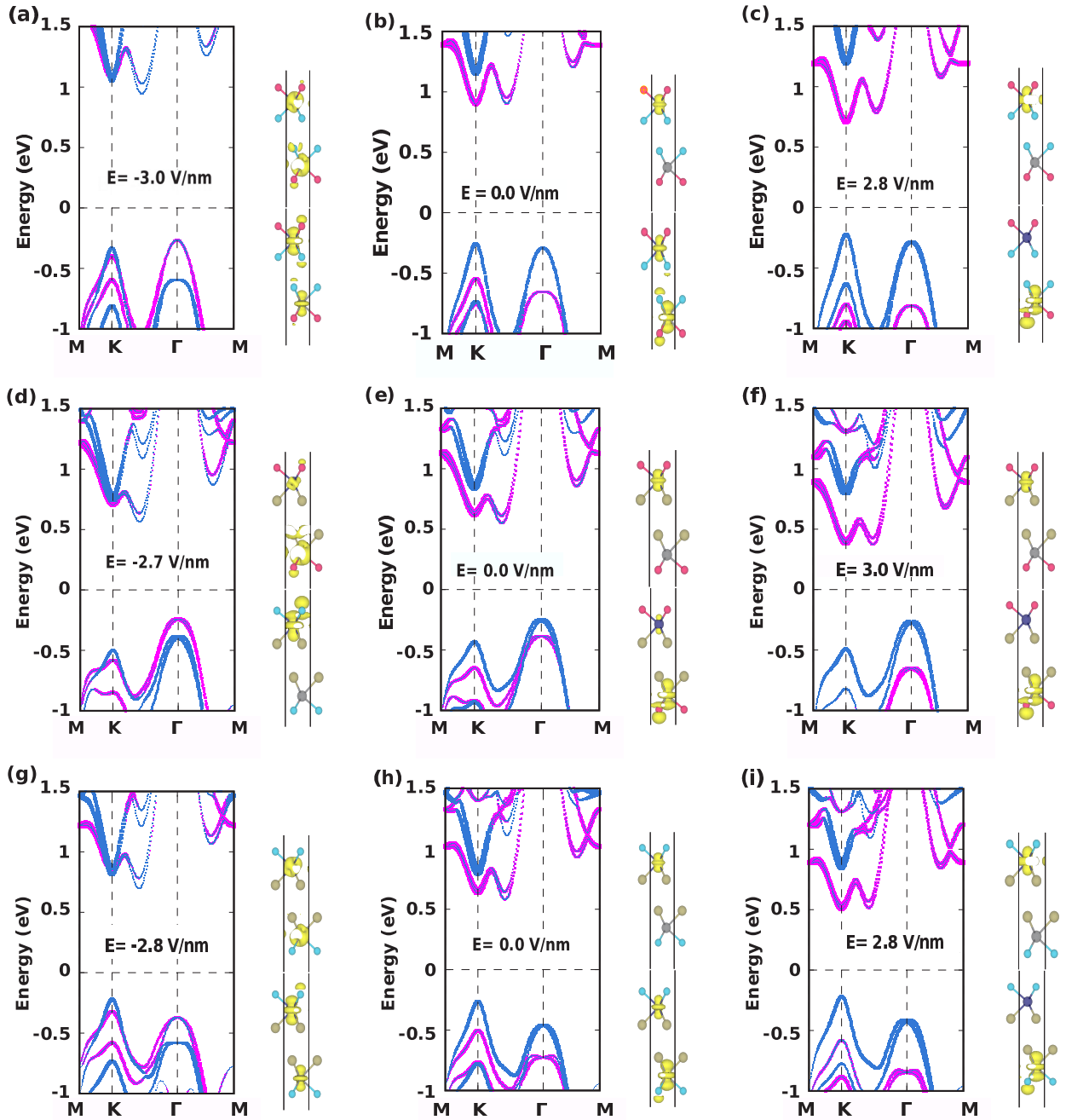
Effects of External Electric Field

FIG. 7. Layer projected band structures and partial charge density plots (band-decomposed charge density plots) under different external electric field strengths for MoSSe/WSSe (upper row), MoSTe/WSTe (middle row), and MoSeTe/WSeTe (bottom row) HSs. The magenta and blue bands denote MoXY and WXY layers, respectively. For all the cases, we plot the charge densities at the Γ point for the valence band (bottom unit cell), while for the conduction band (upper unit cell), we plot charge densities at the K point under zero and positive EEF, and at CBM, which is located in between Γ and K points, under reverse EEF. Isosurface value is set at $0.002e/\text{Å}^3$ for charge density plots. Depending on the relative orientations of EEF and E_{int}, charges (yellow) accumulate or deplete from the WXY bottom layer. Moreover, the layer-projected band structures indicate that the type-II band alignment in the pristine HSs remains robust under a positive electric field, whereas the nature of the band alignment changes by the application of a reverse electric field.

chosen stacking of MoSSe/WSSe HS, and it increases with increasing EEF. Naturally, we also expect that α_R should increase with the strength of the electric field. In AB stacking with a Y-Y interface, the intrinsic electric field is small, which

superimposes with EEF and amplifies α_R. In the case of J-MLs, the Rashba parameter increases with the atomic number of Y atom [65]. The value of α_R for MSeTe (M = Mo or W) is the highest, while for MSSe, it is the lowest since the SOC
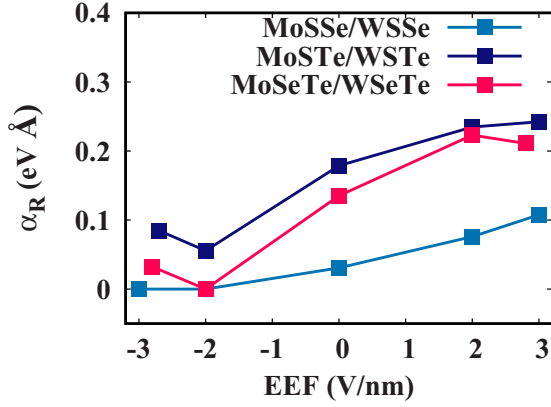
FIG. 8. Variation of the Rashba parameter α_R with EEF. As seen, α_R increases with increasing EEF. In the AB-stacked HSs with Y-Y interface, the small intrinsic electric field superimposes with positive EEF and amplifies α_R.
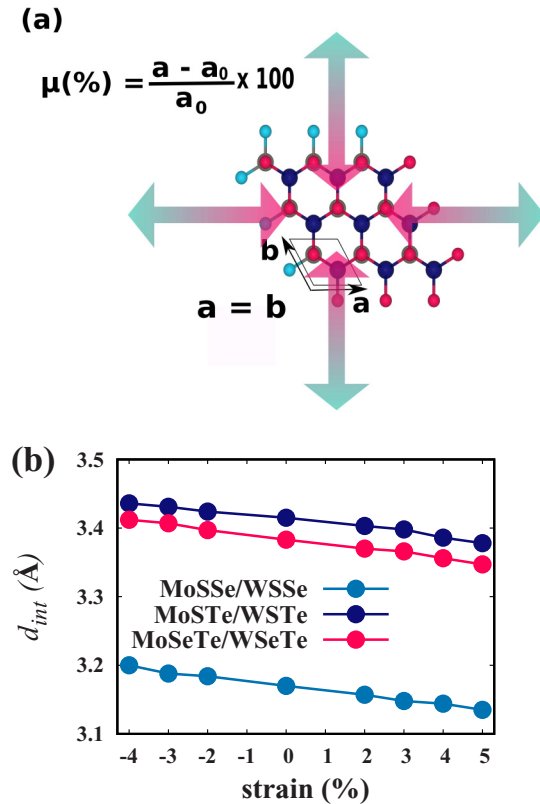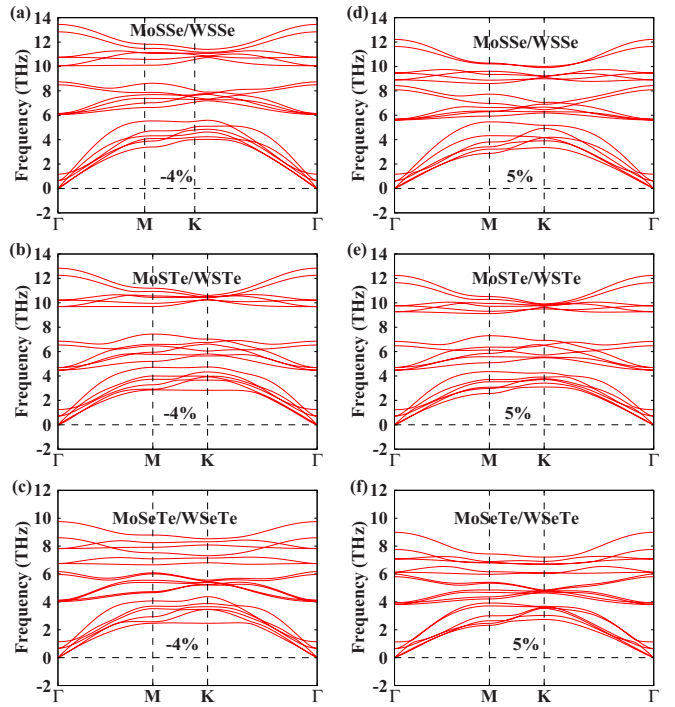

FIG. 10. Phonon dispersions for all three HSs at the largest (a)–(c) compressive and (d)–(f) tensile strains. The phonon frequencies remain positive for the HSs at the maximum strains showing their dynamical stability.

strength is higher for atoms with larger atomic numbers [9]. Therefore, it is expected that the MoSeTe/WSeTe HS would possess the highest α_R. Now, let us compare the difference of electronegativities (Δ_{en}) between different combinations of X and Y. We find that Te-S has the largest Δ_{en}, which results in the highest dipole moments due to chalcogen atoms in the opposite directions from the interface. This mechanism further results in the increment in the distance between the transition metals of both layers, which gives rise to an enhanced net dipole moment (net intrinsic electric field), and consequently highest α_R in AB-stacked MoSTe/WSTe HS.

D. Effects of strain

An in-plane biaxial strain is applied to further investigate the manipulation of the band gap and the Rashba spin splitting in J-HSs. The schematic for this is shown in Fig. 9(a). The strain is applied from -4% to $+5\%$, where negative (positive) means compressive (tensile) strain. We also present the variation of interfacial distances d_{int} with strain in Fig. 9(b), which shows a monotonic decrease of the interlayer distances. We find that d_{int} for $\pm4\%$ strains are not much different ($\sim\pm0.03$ Å) from that of the equilibrium structures. In Fig. S3(a) [70] we show the ground-state energies of the systems under different strains. The system energies remain negative throughout the range of the strains considered. In order to check the dynamical stability of the systems, we also perform phonon calculations under the largest compressive [Figs. 10(a)–10(c)] and tensile strains [Figs. 10(d)–10(f)] applied in our study, and we find no imaginary frequency in the phonon spectra. This suggests that we are safe in applying the

FIG. 9. (a) Schematics for applying an in-plane biaxial strain in our AB-stacked HSs. The pink inward (green outward) arrow depicts the compressive (tensile) strain. a and b are the lattice parameters in the x and y directions, respectively, which are equally compressed and stretched when applying a biaxial strain. μ is the strength of the biaxial strain, a_0 and a are the in-plane lattice parameters of the strained and unstrained structures, respectively. (b) Variation of the distance between the chalcogen atoms at the interface (d_{int}) as a function of biaxial strain. Negative and positive values of the strain represent the compressive and the tensile strains, respectively. d_{int} decreases (increases) linearly with tensile (compressive) strain.
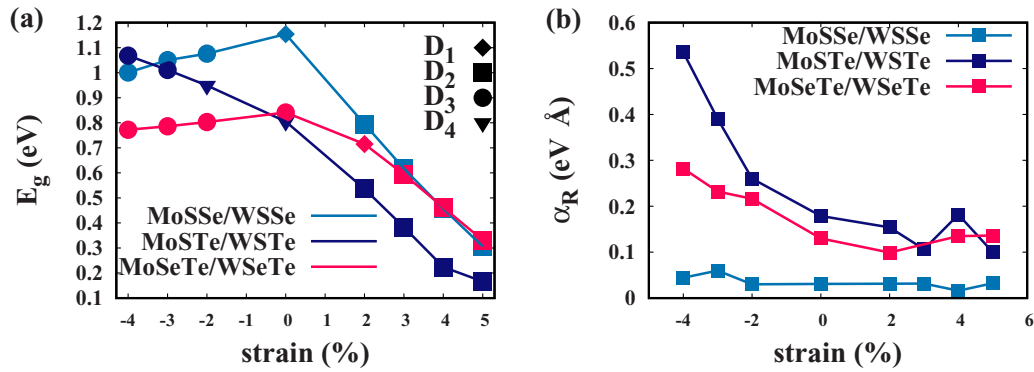
FIG. 11. Evolution of (a) band gap and (b) Rashba parameter as a function of strain. Different symbols represent different types of gaps shown in Fig. 3(d) and different colors correspond to different vdW HSs. MoSTe/WSTe HS shows the highest α_R at 4% compressive strain.

specified ranges of compressive and tensile strains on these heterostructures. In a study by Guo *et al.* [39], electronic properties of Janus MoSSe/WSSe are investigated under 10% compressive strain to 10% tensile biaxial strain. Their calculated values of Young's modulus and Poisson's ratio also show the mechanical stability of the systems. The band gap and

the evolution of Rashba splitting are studied with the band structures under the biaxial strain. The band-gap evolution as a function of strain is plotted in Fig. 11(a). It should be noted that for MoSSe/WSSe and MoSeTe/WSeTe HSs, both tensile and compressive strains reduce the band gaps. Except for the zero strain condition, all the band gaps in the case of

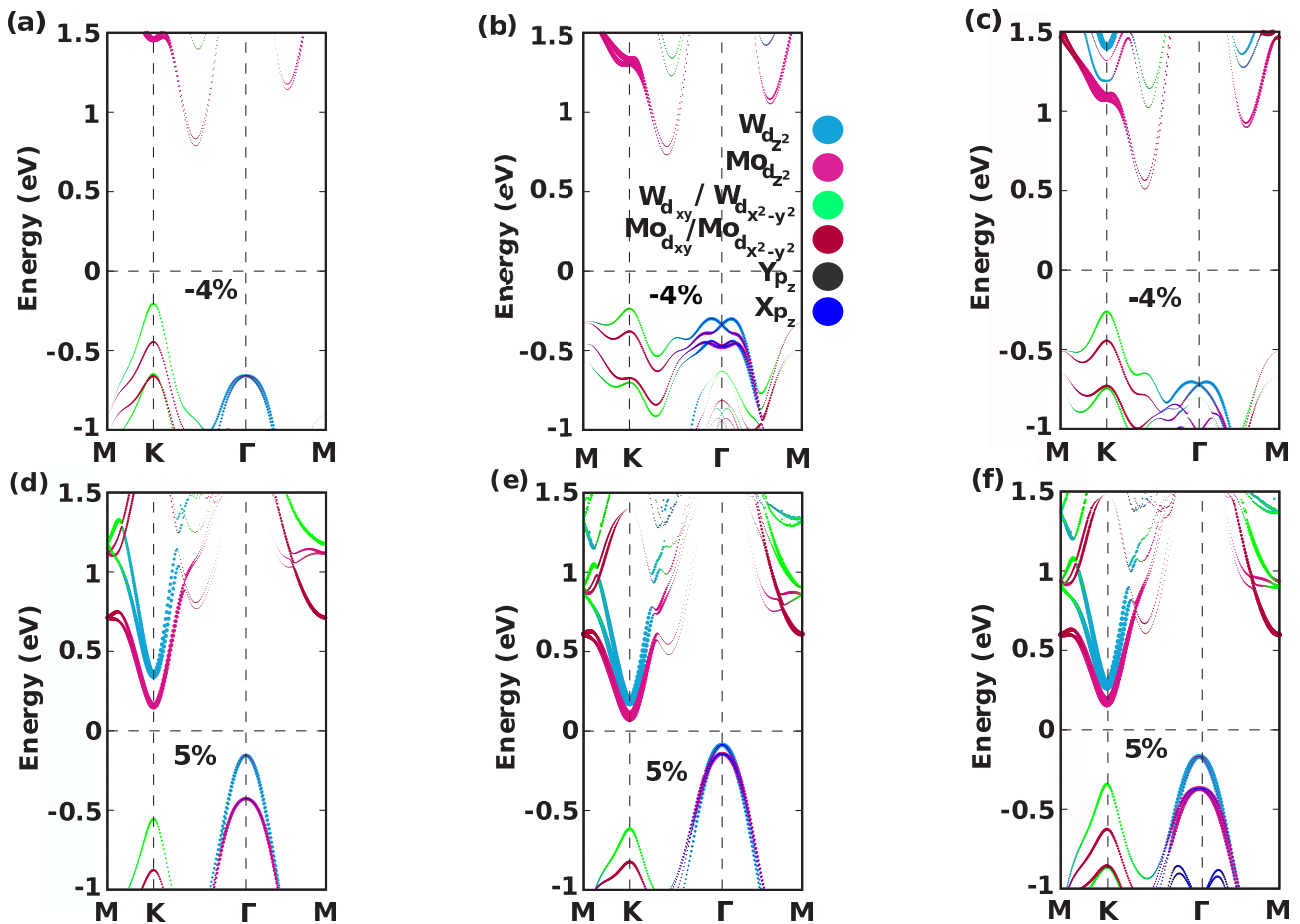## Effects of in-plane Biaxial Strains

FIG. 12. Projected band structures under -4% (upper row) and 5% (lower row) biaxial strains for MoSSe/WSSe, MoSTe/WSTe, and MoSeTe/WSeTe, respectively, from left to right. The weight of the orbitals is defined by the circles of different colors shown in the upper panel. In all cases, the CBM and VBM are located at the MoXY and WXY layers, respectively, confirming that the type-II band alignment remains robust under biaxial strains.

MoSSe/WSSe HS are indirect. Under compressive strain, the band gap is D_3 type, and for tensile strain, it is D_2 type for the MoSSe/WSSe HS. For the MoSTe/WSTe, the VBM moves from the K point at 4% compressive strain to the Γ point at -3% to 5% strains, while the CBM transfers to the K point from the place in between K and Γ points. This is the same case in MoSeTe/WSeTe HS, except the VBM, takes over the Γ point at 4% tensile strain. Therefore, we conclude that in all the HSs, there is a transition in band gaps from the D_3 type to the D_2 type.

Furthermore, it can be realized from Fig. 11(a) that the band gaps will reduce all the way down to zero if the tensile strain is increased enough. A semiconductor to metal transition can be easily seen under higher tensile strain conditions in all three HSs. The band structures at maximum compressive and tensile strains are presented in Fig. 12 along with their orbital weights, which shows that under both tensile and compressive strains, the type-II band alignment of the HSs remains robust. We show the variation of band gap with HSE06 XC functional in Fig. S3(b). The change in the band gap for MoSSe/WSSe under compressive strain is not monotonic. It increases first and then decreases, as shown in Fig. S3(b), while it is clear from Fig. 11(a) that the band gap drops down under the compressive and the tensile strains with the PBE functional. On the other hand, the MoSeTe/WSeTe HS remains a direct band-gap semiconductor until 4% of tensile strain with HSE06 and then changes its nature to an indirect D_2 type gap, in which the VBM at the Γ point goes up in energy than the K point.

Modulation of the Rashba parameter α_R as a function of biaxial strain is demonstrated in Fig. 11(b), which shows that tensile strain suppresses α_R, while a compressive strain enhances it significantly. The interlayer (or interfacial) distance and the net dipole moment are the lowest for the MoSSe/WSSe HS and the highest for the MoSTe/WSTe HS. As seen in Fig. 9(b), the interlayer distance reduces under tensile strain, and it clarifies the reduction in α_R under tensile strain. The smaller interlayer distance reduces the effective dipole moment between the layers and, consequently, the effective intrinsic electric field. On the other hand, a compressive strain increases the interlayer distance, which gives rise to the enhancement in α_R. In the case of MoSTe/WSTe HS, the value of α_R is 178.8 meV Å which increases significantly and reaches 535.3 meV Å with 4% of compressive strain. On the other hand, the MoSSe/WSSe HS is almost insensitive to the in-plane biaxial strain. This large Rashba splitting under 4% compressive strain will have useful applications in experimental devices.

IV. CONCLUSIONS

To summarize, the structural, electronic, and spintronic properties of Janus AB-stacked MoXY/WXY heterostructures

with Y-Y interface have been investigated under external electric field and in-plane biaxial strain using first-principles calculations. We have studied the evolution of the band gap and Rashba parameter α_R for three different vdW HSs of this particular stacking and found the varying natures of band gap and α_R. The MoSSe/WSSe HS shows a direct band gap at the K point under equilibrium state and positive EEF, while it is indirect under reverse EEF and both compressive and tensile strain conditions. The MoSTe/WSTe HS remains an indirect band-gap semiconductor of D_4 type throughout the range of EEF. The nature of the indirect band gap in this HS is different under compressive and tensile strains. The MoSeTe/WSeTe HS shows a direct band gap at 0.28 V/Å and 2% of tensile strain, and it possesses different natures of band gap above and below this 2% strain. All the HSs tend to a semiconductor to metal transition under large tensile strains. This kind of band-gap engineering can be beneficial in nanoelectronics, excitonic physics, and valleytronics. Introduction of a HSE06 XC functional is found to improve (as expected) the band gaps significantly for all the HSs without a noticeable change in the qualitative nature of the bands. Calculations of the Rashba parameter show that α_R is the lowest for the MoSSe/WSSe HS, zero under reverse EEF, and remains almost insensitive to the strain. We note a considerable increment in α_R for the MoSTe/WSTe HS under 4% compressive strain. Our results predict that a small α_R in AB-stacked Janus MoXY/WXY with a Y-Y interface can be enhanced with the effect of an in-plane biaxial strain and can be utilized in the spintronic devices. The type-II band alignment, which results in the long lifetime of carriers, remains robust under biaxial strains and positive electric field, while its nature changes under reverse electric field. Thus, our work describes a way to control the electronic, spintronic, and optoelectronic properties of Janus vdW HSs, which have a strong bearing on potential technological applications. Manipulations of valley degree of freedom and optical properties of these kinds of Janus HSs are still under investigation, leading to new possibilities in the field of valleytronics and optoelectronics. Our DFT calculations for the pristine HSs are supplemented with $\mathbf{k} \cdot \mathbf{p}$ model analyses. We define the minimal $\mathbf{k} \cdot \mathbf{p}$ Hamiltonians around the Γ and K points in the Brillouin zone and numerically fit the DFT bands to study the electronic and spin properties in detail.

ACKNOWLEDGMENTS

[1] A. H. Castro Neto, F. Guinea, N. M. R. Peres, K. S. Novoselov, and A. K. Geim, The electronic properties of graphene, Rev. Mod. Phys. **81**, 109 (2009).

[2] Y.-H. Lee, X.-Q. Zhang, W. Zhang, M.-T. Chang, C.-T. Lin, K.-D. Chang, Y.-C. Yu, J. T.-W. Wang, C.-S. Chang, L.-J. Li *et al.*, Synthesis of large-area MoS$_2$ atomic layers with chemical vapor deposition, Adv. Mater. **24**, 2320 (2012).

[3] Y. Shi, H. Li, and L.-J. Li, Recent advances in controlled synthesis of two-dimensional transition metal dichalcogenides

via vapour deposition techniques, Chem. Soc. Rev. **44**, 2744 (2015).

[4] H. Li, G. Lu, Y. Wang, Z. Yin, C. Cong, Q. He, L. Wang, F. Ding, T. Yu, and H. Zhang, Mechanical exfoliation and characterization of single-and few-layer nanosheets of WSe_2, TaS_2, and $TaSe_2$, Small **9**, 1974 (2013).

[5] Z. Zeng, T. Sun, J. Zhu, X. Huang, Z. Yin, G. Lu, Z. Fan, Q. Yan, H. H. Hng, and H. Zhang, An effective method for the fabrication of few-layer-thick inorganic nanosheets, Angew. Chem. Int. Ed. **51**, 9052 (2012).

[6] Q. Feng, N. Mao, J. Wu, H. Xu, C. Wang, J. Zhang, and L. Xie, Growth of $MoS_{2(1-x)}Se_{2x}$ ($x = 0.41–1.00$) monolayer alloys with controlled morphology by physical vapor deposition, ACS Nano **9**, 7450 (2015).

[7] J. N. Coleman, M. Lotya, A. O'Neill, S. D. Bergin, P. J. King, U. Khan, K. Young, A. Gaucher, S. De, R. J. Smith *et al.*, Two-dimensional nanosheets produced by liquid exfoliation of layered materials, Science **331**, 568 (2011).

[8] R. Li, Y. Cheng, and W. Huang, Recent progress of Janus 2D transition metal chalcogenides: From theory to experiments, Small **14**, 1802091 (2018).

[9] Y. Cheng, Z. Zhu, M. Tahir, and U. Schwingenschlögl, Spin-orbit–induced spin splittings in polar transition metal dichalcogenide monolayers, Europhys. Lett. **102**, 57001 (2013).

[10] A.-Y. Lu, H. Zhu, J. Xiao, C.-P. Chuu, Y. Han, M.-H. Chiu, C.-C. Cheng, C.-W. Yang, K.-H. Wei, Y. Yang *et al.*, Janus monolayers of transition metal dichalcogenides, Nat. Nanotechnol. **12**, 744 (2017).

[11] J. Zhang, S. Jia, I. Kholmanov, L. Dong, D. Er, W. Chen, H. Guo, Z. Jin, V. B. Shenoy, L. Shi *et al.*, Janus monolayer transition-metal dichalcogenides, ACS Nano **11**, 8192 (2017).

[12] Y.-C. Lin, C. Liu, Y. Yu, E. Zarkadoula, M. Yoon, A. A. Puretzky, L. Liang, X. Kong, Y. Gu, A. Strasser *et al.*, Low energy implantation into transition-metal dichalcogenide monolayers to form Janus structures, ACS Nano **14**, 3896 (2020).

[13] G. Dresselhaus, Spin-orbit coupling effects in zinc blende structures, Phys. Rev. **100**, 580 (1955).

[14] Y. A. Bychkov and É. I. Rashba, Properties of a 2D electron gas with lifted spectral degeneracy, Sov. J. Exper. Theor. Phys. Lett. **39**, 78 (1984).

[15] A. Manchon, H. C. Koo, J. Nitta, S. Frolov, and R. Duine, New perspectives for Rashba spin–orbit coupling, Nat. Mater. **14**, 871 (2015).

[16] G. Bihlmayer, O. Rader, and R. Winkler, Focus on the Rashba effect, New J. Phys. **17**, 050202 (2015).

[17] A. C. Riis-Jensen, T. Deilmann, T. Olsen, and K. S. Thygesen, Classifying the electronic and optical properties of Janus monolayers, ACS Nano **13**, 13354 (2019).

[18] W. Li and J. Li, Piezoelectricity in two-dimensional group-III monochalcogenides, Nano Res. **8**, 3796 (2015).

[19] L. Dong, J. Lou, and V. B. Shenoy, Large in-plane and vertical piezoelectricity in Janus transition metal dichalchogenides, ACS Nano **11**, 8242 (2017).

[20] M. Yagmurcukardes, C. Sevik, and F. M. Peeters, Electronic, vibrational, elastic, and piezoelectric properties of monolayer Janus MoSTe phases: A first-principles study, Phys. Rev. B **100**, 045415 (2019).

[21] M. Sato and S. Fujimoto, Topological phases of noncentrosymmetric superconductors: Edge states, Majorana fermions, and non-Abelian statistics, Phys. Rev. B **79**, 094504 (2009).

[22] A. B. Maghirang, Z.-Q. Huang, R. A. B. Villaos, C.-H. Hsu, L.-Y. Feng, E. Florido, H. Lin, A. Bansil, and F.-C. Chuang, Predicting two-dimensional topological phases in Janus materials by substitutional doping in transition metal dichalcogenide monolayers, npj 2D Mater. Appl. **3**, 35 (2019).

[23] D. Dey and A. S. Botana, Structural, electronic, and magnetic properties of vanadium-based Janus dichalcogenide monolayers: A first-principles study, Phys. Rev. Materials **4**, 074002 (2020).

[24] T. Georgiou, R. Jalil, B. D. Belle, L. Britnell, R. V. Gorbachev, S. V. Morozov, Y.-J. Kim, A. Gholinia, S. J. Haigh, O. Makarovsky *et al.*, Vertical field-effect transistor based on graphene–WS_2 heterostructures for flexible and transparent electronics, Nat. Nanotechnol. **8**, 100 (2013).

[25] A. Anto Jeffery, C. Nethravathi, and M. Rajamathi, Two-dimensional nanosheets and layered hybrids of MoS_2 and WS_2 through exfoliation of ammoniated MS_2 (M= Mo, W), J. Phys. Chem. C **118**, 1386 (2014).

[26] B. Zheng, C. Ma, D. Li, J. Lan, Z. Zhang, X. Sun, W. Zheng, T. Yang, C. Zhu, G. Ouyang *et al.*, Band alignment engineering in two-dimensional lateral heterostructures, J. Am. Chem. Soc. **140**, 11193 (2018).

[27] L. Kou, T. Frauenheim, and C. Chen, Nanoscale multilayer transition-metal dichalcogenide heterostructures: Band gap modulation by interfacial strain and spontaneous polarization, J. Phys. Chem. Lett. **4**, 1730 (2013).

[28] H.-P. Komsa and A. V. Krasheninnikov, Electronic structures and optical properties of realistic transition metal dichalcogenide heterostructures from first principles, Phys. Rev. B **88**, 085318 (2013).

[29] H. Terrones, F. López-Urías, and M. Terrones, Novel hetero-layered materials with tunable direct band gaps by sandwiching different metal disulfides and diselenides, Sci. Rep. **3**, 1549 (2013).

[30] R. Long and O. V. Prezhdo, Quantum coherence facilitates efficient charge separation at a MoS_2/$MoSe_2$ van der Waals junction, Nano Lett. **16**, 1996 (2016).

[31] M. Chhowalla, H. S. Shin, G. Eda, L.-J. Li, K. P. Loh, and H. Zhang, The chemistry of two-dimensional layered transition metal dichalcogenide nanosheets, Nat. Chem. **5**, 263 (2013).

[32] L. Kou, A. Du, C. Chen, and T. Frauenheim, Strain engineering of selective chemical adsorption on monolayer MoS_2, Nanoscale **6**, 5156 (2014).

[33] A. Arora, M. Drüppel, R. Schmidt, T. Deilmann, R. Schneider, M. R. Molas, P. Marauhn, S. M. de Vasconcellos, M. Potemski, M. Rohlfing, and R. Bratschitsch, Interlayer excitons in a bulk van der Waals semiconductor, Nat. Commun. **8**, 639 (2017).

[34] H. Liu, Y.-X. Zong, P. Wang, H. Wen, H.-B. Wu, J.-B. Xia, and Z. Wei, Excitons in two-dimensional van der Waals heterostructures, J. Phys. D: Appl. Phys. **54**, 053001 (2020).

[35] R. Suzuki, M. Sakano, Y. Zhang, R. Akashi, D. Morikawa, A. Harasawa, K. Yaji, K. Kuroda, K. Miyamoto, T. Okuda *et al.*, Valley-dependent spin polarization in bulk MoS_2 with broken inversion symmetry, Nat. Nanotechnol. **9**, 611 (2014).

[36] F. Li, W. Wei, P. Zhao, B. Huang, and Y. Dai, Electronic and optical properties of pristine and vertical and lateral heterostructures of Janus MoSSe and WSSe, J. Phys. Chem. Lett. **8**, 5959 (2017).

[37] W. Zhou, J. Chen, Z. Yang, J. Liu, and F. Ouyang, Geometry and electronic structure of monolayer, bilayer, and multilayer Janus WSSe, Phys. Rev. B **99**, 075160 (2019).

[38] A. Rezavand and N. Ghobadi, Stacking-dependent Rashba spin-splitting in Janus bilayer transition metal dichalcogenides: The role of in-plane strain and out-of-plane electric field, Phys. E **132**, 114768 (2021).

[39] W. Guo, X. Ge, S. Sun, Y. Xie, and X. Ye, The strain effect on the electronic properties of the MoSSe/WSSe van der Waals heterostructure: A first-principles study, Phys. Chem. Chem. Phys. **22**, 4946 (2020).

[40] Y. Wang, W. Wei, B. Huang, and Y. Dai, The mirror asymmetry induced nontrivial properties of polar WSSe/MoSSe heterostructures, J. Phys.: Condens. Matter **31**, 125003 (2019).

[41] J. E. Hirsch, Spin Hall Effect, Phys. Rev. Lett. **83**, 1834 (1999).

[42] J. Sinova, D. Culcer, Q. Niu, N. A. Sinitsyn, T. Jungwirth, and A. H. MacDonald, Universal Intrinsic Spin Hall Effect, Phys. Rev. Lett. **92**, 126603 (2004).

[43] H. Wang, P. Gopal, S. Picozzi, S. Curtarolo, M. B. Nardelli, and J. Sławińska, Spin Hall effect in prototype Rashba ferroelectrics GeTe and SnTe, npj Comput. Mater. **6**, 7 (2020).

[44] S.-B. Yu, M. Zhou, D. Zhang, and K. Chang, Spin Hall effect in the monolayer Janus compound MoSSe enhanced by Rashba spin-orbit coupling, Phys. Rev. B **104**, 075435 (2021).

[45] S. Datta and B. Das, Electronic analog of the electro-optic modulator, Appl. Phys. Lett. **56**, 665 (1990).

[46] K. V. Shanavas and S. Satpathy, Electric Field Tuning of the Rashba Effect in the Polar Perovskite Structures, Phys. Rev. Lett. **112**, 086802 (2014).

[47] M.-Y. Liu, L. Gong, Y. He, and C. Cao, Tuning Rashba effect, band inversion, and spin-charge conversion of Janus XSn$_2Y$ monolayers via an external field, Phys. Rev. B **103**, 075421 (2021).

[48] S. Singh and A. H. Romero, Giant tunable Rashba spin splitting in a two-dimensional BiSb monolayer and in BiSb/AlN heterostructures, Phys. Rev. B **95**, 165444 (2017).

[49] M. A. U. Absor, I. Santoso, Harsojo, K. Abraha, H. Kotaka, F. Ishii, and M. Saito, Strong Rashba effect in the localized impurity states of halogen-doped monolayer PtSe$_2$, Phys. Rev. B **97**, 205138 (2018).

[50] J. Chen, K. Wu, H. Ma, W. Hu, and J. Yang, Tunable Rashba spin splitting in Janus transition-metal dichalcogenide monolayers via charge doping, RSC Adv. **10**, 6388 (2020).

[51] G. Kresse and J. Furthmüller, Efficiency of ab-initio total energy calculations for metals and semiconductors using a plane-wave basis set, Comput. Mater. Sci. **6**, 15 (1996).

[52] G. Kresse and J. Furthmüller, Efficient iterative schemes for *ab initio* total-energy calculations using a plane-wave basis set, Phys. Rev. B **54**, 11169 (1996).

[53] J. P. Perdew, K. Burke, and M. Ernzerhof, Generalized Gradient Approximation Made Simple, Phys. Rev. Lett. **77**, 3865 (1996).

[54] P. E. Blöchl, Projector augmented-wave method, Phys. Rev. B **50**, 17953 (1994).

[55] G. Kresse and D. Joubert, From ultrasoft pseudopotentials to the projector augmented-wave method, Phys. Rev. B **59**, 1758 (1999).

[56] J. Heyd, G. E. Scuseria, and M. Ernzerhof, Hybrid functionals based on a screened Coulomb potential, J. Chem. Phys. **118**, 8207 (2003).

[57] J. Heyd and G. E. Scuseria, Efficient hybrid density functional calculations in solids: Assessment of the Heyd–Scuseria–Ernzerhof screened Coulomb hybrid functional, J. Chem. Phys. **121**, 1187 (2004).

[58] S. Grimme, Semiempirical GGA-type density functional constructed with a long-range dispersion correction, J. Comput. Chem. **27**, 1787 (2006).

[59] A. Togo and I. Tanaka, First principles phonon calculations in materials science, Scr. Mater. **108**, 1 (2015).

[60] J. Neugebauer and M. Scheffler, Adsorbate-substrate and adsorbate-adsorbate interactions of Na and K adlayers on Al (111), Phys. Rev. B **46**, 16067 (1992).

[61] K. Momma and F. Izumi, Vesta 3 for three-dimensional visualization of crystal, volumetric and morphology data, J. Appl. Cryst. **44**, 1272 (2011).

[62] F. Wypych, T. Weber, and R. Prins, Scanning tunneling microscopic investigation of 1T-MoS$_2$, Chem. Mater. **10**, 723 (1998).

[63] X. Tang, S. Li, Y. Ma, A. Du, T. Liao, Y. Gu, and L. Kou, Distorted Janus transition metal dichalcogenides: Stable two-dimensional materials with sizable band gap and ultrahigh carrier mobility, J. Phys. Chem. C **122**, 19153 (2018).

[64] X. Yang, D. Singh, Z. Xu, Z. Wang, and R. Ahuja, An emerging Janus MoSeTe material for potential applications in optoelectronic devices, J. Mater. Chem. C **7**, 12312 (2019).

[65] T. Hu, F. Jia, G. Zhao, J. Wu, A. Stroppa, and W. Ren, Intrinsic and anisotropic Rashba spin splitting in Janus transition-metal dichalcogenide monolayers, Phys. Rev. B **97**, 235404 (2018).

[66] C. Xia, W. Xiong, J. Du, T. Wang, Y. Peng, and J. Li, Universality of electronic characteristics and photocatalyst applications in the two-dimensional Janus transition metal dichalcogenides, Phys. Rev. B **98**, 165424 (2018).

[67] F. Wang, J. Wang, S. Guo, J. Zhang, Z. Hu, and J. Chu, Tuning coupling behavior of stacked heterostructures based on MoS$_2$, WS$_2$, and WSe$_2$, Sci. Rep. **7**, 44712 (2017).

[68] S. W. Han, H. Kwon, S. K. Kim, S. Ryu, W. S. Yun, D. H. Kim, J. H. Hwang, J.-S. Kang, J. Baik, H. J. Shin, and S. C. Hong, Band-gap transition induced by interlayer van der Waals interaction in MoS$_2$, Phys. Rev. B **84**, 045409 (2011).

[69] S. Sahoo, M. C. Sahu, S. K. Mallik, N. K. Sharma, A. K. Jena, S. K. Gupta, R. Ahuja, and S. Sahoo, Electric field-modulated charge transfer in geometrically tailored MoX$_2$/WX$_2$ (X= S, Se) heterostructures, J. Phys. Chem. C **125**, 22360 (2021).

[70] See Supplemental Material at http://link.aps.org/supplemental/10.1103/PhysRevB.106.035125 for detailed information about calculations with HSE06 hybrid functional.

[71] X. Hong, J. Kim, S.-F. Shi, Y. Zhang, C. Jin, Y. Sun, S. Tongay, J. Wu, Y. Zhang, and F. Wang, Ultrafast charge transfer in atomically thin MoS$_2$/WS$_2$ heterostructures, Nat. Nanotechnol. **9**, 682 (2014).

[72] H. Yu, X. Cui, X. Xu, and W. Yao, Valley excitons in two-dimensional semiconductors, Natl. Sci. Rev. **2**, 57 (2015).

[73] Z. Guan, S. Ni, and S. Hu, Tunable electronic and optical properties of monolayer and multilayer janus mosse as a photocatalyst for solar water splitting: A first-principles study, J. Phys. Chem. C **122**, 6209 (2018).

[74] W. J. Yu, Y. Liu, H. Zhou, A. Yin, Z. Li, Y. Huang, and X. Duan, Highly efficient gate-tunable photocurrent generation in vertical heterostructures of layered materials, Nat. Nanotechnol. **8**, 952 (2013).

[75] D. Xiao, G.-B. Liu, W. Feng, X. Xu, and W. Yao, Coupled Spin and Valley Physics in Monolayers of MoS₂ and Other Group-VI Dichalcogenides, Phys. Rev. Lett. **108**, 196802 (2012).

[76] K. Kośmider, J. W. González, and J. Fernández-Rossier, Large spin splitting in the conduction band of transition metal dichalcogenide monolayers, Phys. Rev. B **88**, 245436 (2013).

[77] H. Yuan, M. S. Bahramy, K. Morimoto, S. Wu, K. Nomura, B.-J. Yang, H. Shimotani, R. Suzuki, M. Toh, C. Kloc *et al.*, Zeeman-type spin splitting controlled by an electric field, Nat. Phys. **9**, 563 (2013).

[78] S. Vajna, E. Simon, A. Szilva, K. Palotas, B. Ujfalussy, and L. Szunyogh, Higher-order contributions to the Rashba-Bychkov effect with application to the Bi/Ag (111) surface alloy, Phys. Rev. B **85**, 075404 (2012).

[79] Q.-F. Yao, J. Cai, W.-Y. Tong, S.-J. Gong, J.-Q. Wang, X. Wan, C.-G. Duan, and J. H. Chu, Manipulation of the large Rashba spin splitting in polar two-dimensional transition-metal dichalcogenides, Phys. Rev. B **95**, 165401 (2017).

[80] A. Kormányos, V. Zólyomi, N. D. Drummond, and G. Burkard, Spin-Orbit Coupling, Quantum Dots, and Qubits in Monolayer Transition Metal Dichalcogenides, Phys. Revi. X **4**, 011034 (2014).

[81] L. L. Tao and E. Y. Tsymbal, Persistent spin texture enforced by symmetry, Nat. Commun. **9**, 2763 (2018).

[82] C. Liu, H. Gao, Y. Li, K. Wang, L. A. Burton, and W. Ren, Manipulation of the Rashba effect in layered tellurides MTe (M= Ge, Sn, Pb), J. Mater. Chem. C **8**, 5143 (2020).

[83] M. Sharma, A. Kumar, P. Ahluwalia, and R. Pandey, Strain and electric field induced electronic properties of two-dimensional hybrid bilayers of transition-metal dichalcogenides, J. Appl. Phys. **116**, 063711 (2014).